CM² MAGAZINE

第 125 期

南方科技大学海洋磁学中心主编

http://cm2.sustech.edu.cn/

创刊词

海洋是生命的摇篮，是文明的纽带。地球上最早的生命诞生于海洋，海洋里的生命最终进化成了人类，人类的文化融合又通过海洋得以实现。人因海而兴。

人类对海洋的探索从未停止。从远古时代美丽的神话传说，到麦哲伦的全球航行，再到现代对大洋的科学钻探计划，海洋逐渐从人类敬畏崇拜幻想的精神寄托演变成可以开发利用与科学研究的客观存在。其中，上个世纪与太空探索同步发展的大洋科学钻探计划将人类对海洋的认知推向了崭新的纬度：深海（deep sea）与深时（deep time）。大洋钻探计划让人类知道，奔流不息的大海之下，埋藏的却是亿万年的地球历史。它们记录了地球板块的运动，从而使板块构造学说得到证实；它们记录了地球环境的演变，从而让古海洋学方兴未艾。

在探索海洋的悠久历史中，从大航海时代的导航，到大洋钻探计划中不可或缺的磁性地层学，磁学发挥了不可替代的作用。这不是偶然，因为从微观到宏观，磁性是最基本的物理属性之一，可以说，万物皆有磁性。基于课题组的学科背景和对海洋的理解，我们对海洋的探索以磁学为主要手段，海洋磁学中心因此而生。

海洋磁学中心，简称 CM^2，一为其全名“Centre for Marine Magnetism”的缩写，另者恰与爱因斯坦著名的质能方程 $E = MC^2$ 对称，借以表达我们对科学巨匠的敬仰和对科学的不懈追求。

然而科学从来不是单打独斗的产物。我们以磁学为研究海洋的主攻利器，但绝不仅限于磁学。凡与磁学相关的领域均是我们关注的重点。为了跟踪反映国内外地球科学特别是与磁学有关的地球科学领域的最新研究进展，海洋磁学中心特地主办 CM^2 Magazine，以期与各位地球科学工作者相互交流学习、合作共进！

“海洋孕育了生命，联通了世界，促进了发展”。21 世纪是海洋科学的时代，由陆向海，让我们携手迈进中国海洋科学的黄金时代。

目录

1. 人类活动导致的营养盐输入对气候驱动下海洋碳和氧循环过程的影响

翻译人：仲义 zhongy@sustech.edu.cn

Yamamoto A, Hajima T, Yamazaki D. ***Competing and accelerating effects of anthropogenic nutrient inputs on climate-driven changes in ocean carbon and oxygen cycles*** *[J] Science Advances, 2022, 8(26), eabl9207.*

https://www.science.org/doi/abs/10.1126/sciadv.abl9207

摘要：人类活动大大增加了从大气和河流向海洋输送的养分。然而，广泛使用 CMIP5 地球系统模型中没有考虑养分输入增加的影响，这将给海洋生物地球化学模型的模拟带来很大的偏差。本文作者利用大气扰动和河流输入的地球系统模型的历史模拟结果，发现人为养分输入对过去全球海洋生物地球化学变化的贡献与气候变化的影响在量级上相似。人类活动的营养盐输入增加海洋生产力和碳的吸收，抵消了气候导致的较少，并加速海洋上部水体由气候驱动的脱氧作用。此外，考虑到人为营养输入会提供已知的碳收支不平衡，同时低估了全球氧库存减少的量。因此，人为营养输入和气候变化的影响对于评估人类对于海洋生物地球化学的影响至关重要。

ABSTRACT: Nutrient inputs from the atmosphere and rivers to the ocean are increased substantially by human activities. However, the effects of increased nutrient inputs are not included in the widely used CMIP5 Earth system models, which introduce bias into model simulations of ocean biogeochemistry. Here, using historical simulations by an Earth system model with perturbed atmospheric and riverine nutrient inputs, we show that the contribution of anthropogenic nutrient inputs to past global changes in ocean biogeochemistry is of similar magnitude to the effect of climate change. Anthropogenic nutrient inputs increase oceanic productivity and carbon uptake, offsetting climate-induced decrease and accelerating climate-driven deoxygenation in the upper ocean. Moreover, accounting for anthropogenic nutrient inputs improves the known carbon budget imbalance and model underestimation of the observed decrease in the global oxygen inventory. Considering the effects of both nutrient inputs and climate change is crucial in assessing anthropogenic impacts on ocean biogeochemistry.

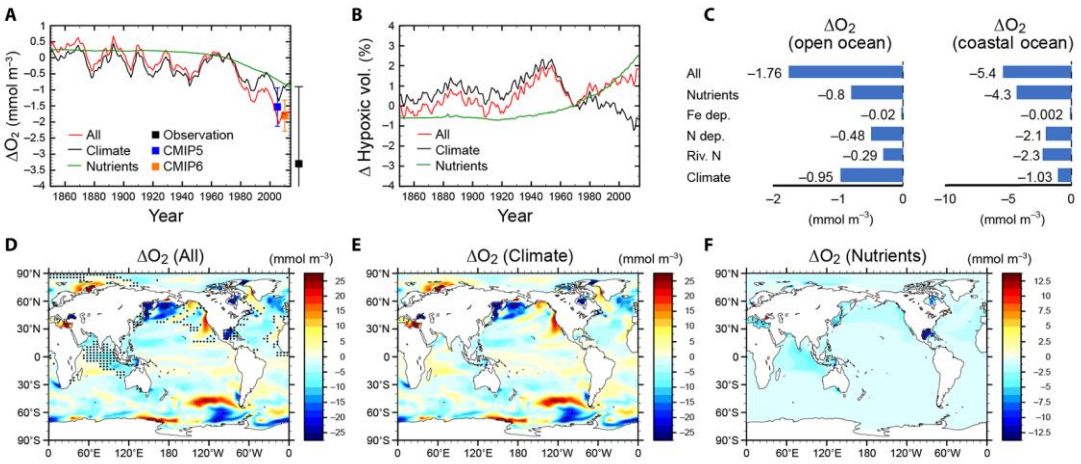

Figure 1. Dissolved oxygen changes. (A) Time series of changes in dissolved oxygen concentration in the upper 1000 m for all, climate, and anthropogenic nutrient effects. Values are anomalies relative to 1970. Observed change from 1970 to 2010 is shown as black square. Historical trends in CMIP5 (1970–2005) and CMIP6 (1970–2010) models are shown as blue and orange squares, respectively. (B) Same as (A) but for the volume of the hypoxic waters. (C) Changes in dissolved oxygen for open (left) and coastal (right) ocean. (D to F) The distributions of changes in dissolved oxygen from 1970 to 2010. The contributions of all effects (D), climate (E), and nutrients (F) were calculated. Stippling indicates the areas in which the nutrient effect is greater than the climate effect. The color scale of (D) and (E) is different from that of (F) by a factor of 2.

2. 印度和亚洲大陆碰撞引起的天山造山带陆内变形

翻译人：周洋 zhouy3@sustech.edu.cn

Li W, Chen Y, Yuan X H, et al. ***Intracontinental deformation of the Tianshan Orogen in response to India-Asia collision*** *[J] Nature Communications, 2022, 13, 3738.*

https://doi.org/10.1038/s41467-022-30795-6

摘要：在远离板块边界的地方，大陆岩石圈如何变形，长期以来一直存在争议。天山是陆内环境中岩石圈变形的典型例子。天山在古生代阿尔泰山增生过程中形成，新生代重新活动，这可能是印度-亚洲大陆碰撞的远场效应。在这里，我们展示了天山中部岩石圈的地震图像，这些图像来自于接收函数和沿 N-S 走向地震测线的瑞利波。在天山内部观察到岩石圈发生广泛变形，浅层地壳脆性变形和莫霍面附近塑性变形。我们发现地壳中保留了早期的多个增生结构，地壳在南部受到纯剪切缩短和北部厚皮构造的影响，同时受到周围地块的阻挡，推覆构造发育有限，莫霍面的平衡剖面支持天山陆内变形。这些发现为天山造山带提供了一个较为统一的地震模型，并证实了印度-亚洲碰撞应力的有效传递导致了陆内造山带的活化。

ABSTRACT: How the continental lithosphere deforms far away from plate boundaries has been long debated. The Tianshan is a type-example of ongoing lithospheric deformation in an intracontinental setting. It formed during the Paleozoic accretion of the Altaids and was rejuvenated in the Cenozoic, which might be a far-field response to the India-Asia collision. Here we present seismic images of the lithosphere across the central Tianshan, which were constructed from receiver functions and Rayleigh wave dispersions along a N–S-trending linear seismic array. We observe an extensively deformed lithosphere in the Tianshan with inherited, structurally controlled brittle deformation in the shallow crust and plastic deformation near the Moho. We find that earlier multiple accretionary structures were preserved in the crust, which was deformed by pure-shear shortening in the south and thick-skinned tectonics in the north but was limitedly underthrusted by surrounding blocks. A balanced cross-section of Moho discontinuities supports the concept that intracontinental deformation in the Tianshan intensified synchronously with the direct contact between the underthrusting Indian slab and the Tarim Craton in the

Late Miocene (~10 Ma). These findings provide a robust and unified seismic model for the Tianshan Orogen, and confirm that effective delivery of the India-Asia collision stress induced the rejuvenation of this intracontinental orogen.

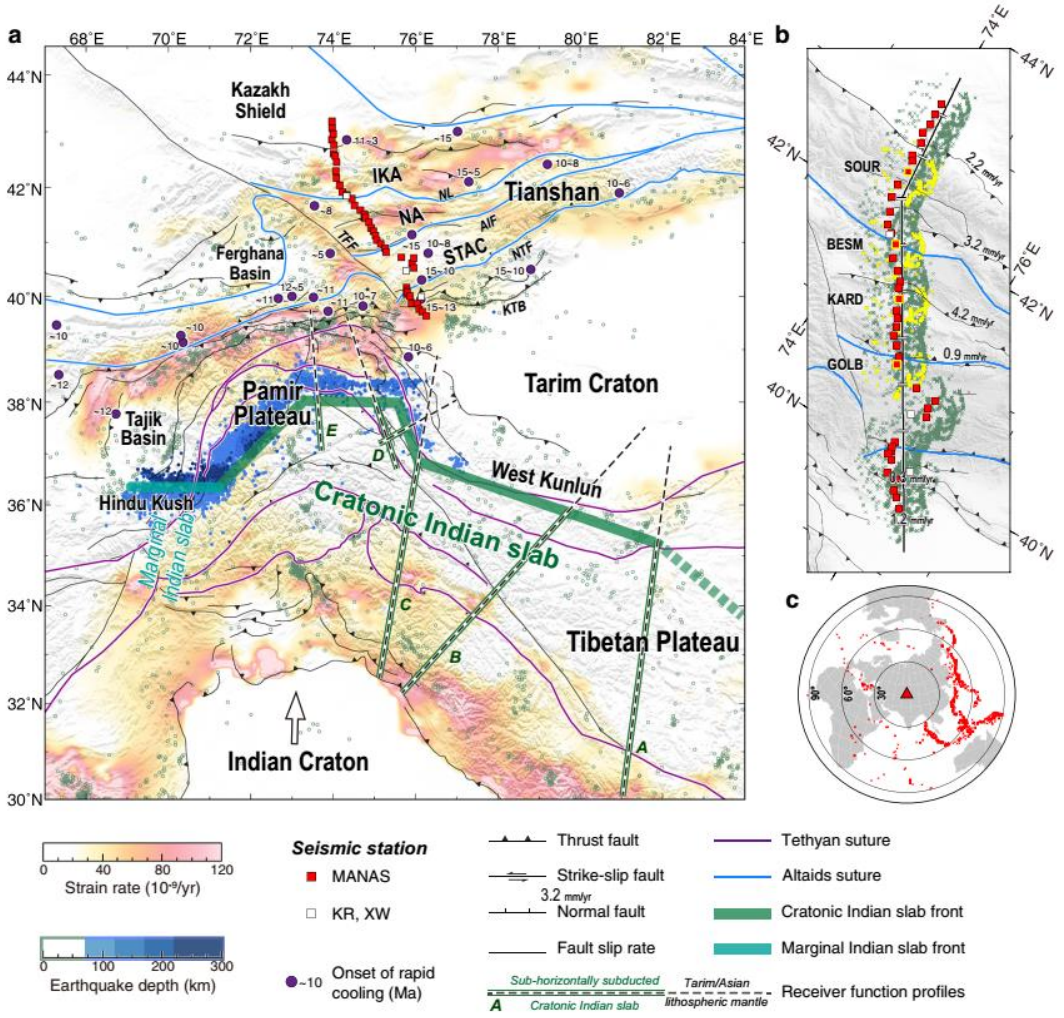

Figure 1. Tectonic setting of the Tianshan and data coverage of the seismic cross-section. a Tectonic map with strain rates inverted from GPS observations. Squares denote seismic stations used in this study from the Middle AsiaN Active Source project (MANAS) and other networks (KR and XW). Green and blue circles show earthquakes at shallow65 (⩽70 km) and intermediate66,67 (70 – 300 km) depths. The purple points with numbers denote the onset of rapid cooling derived from thermochronological studies. The present-day northern front of the Indian slab, including the marginal Indian slab beneath the Hindu Kush and the cratonic Indian slab beneath the Pamir Plateau and the western Tibetan Plateau are together constrained by the interpretations of the previous receiver function profiles (A: Zhao et al.31, B: Rai et al.30, C: Kumar et al.29, D: Xu et al.33, E: Schneider et al.32). Sutures in the Altaids and the Tethyan tectonic domain are marked with light

blue and purple lines, respectively, and major faults are in black lines (Central Asia Fault Database 68). AIF Atbashy-Inylchek Fault, IKA Issyk Kul Arc, NA Naryn Arc, NL Nikolaev Line, NTF North Tarim Fault, KTB Kepingtag Thrust Belt, STAC South Tianshan Accretionary Complex, TFF Talas-Ferghana Fault. b Stations and piercing points of the Ps phases at a depth of 60 km along the crosssection are indicated by solid lines with 50-km scale marks. Numbers denote fault slip rates. Sample stations GOLB, KARD, BESM, and SOUR are highlighted by yellow frames, for which inversions are shown in the supplement. c Distribution of events used in this study.

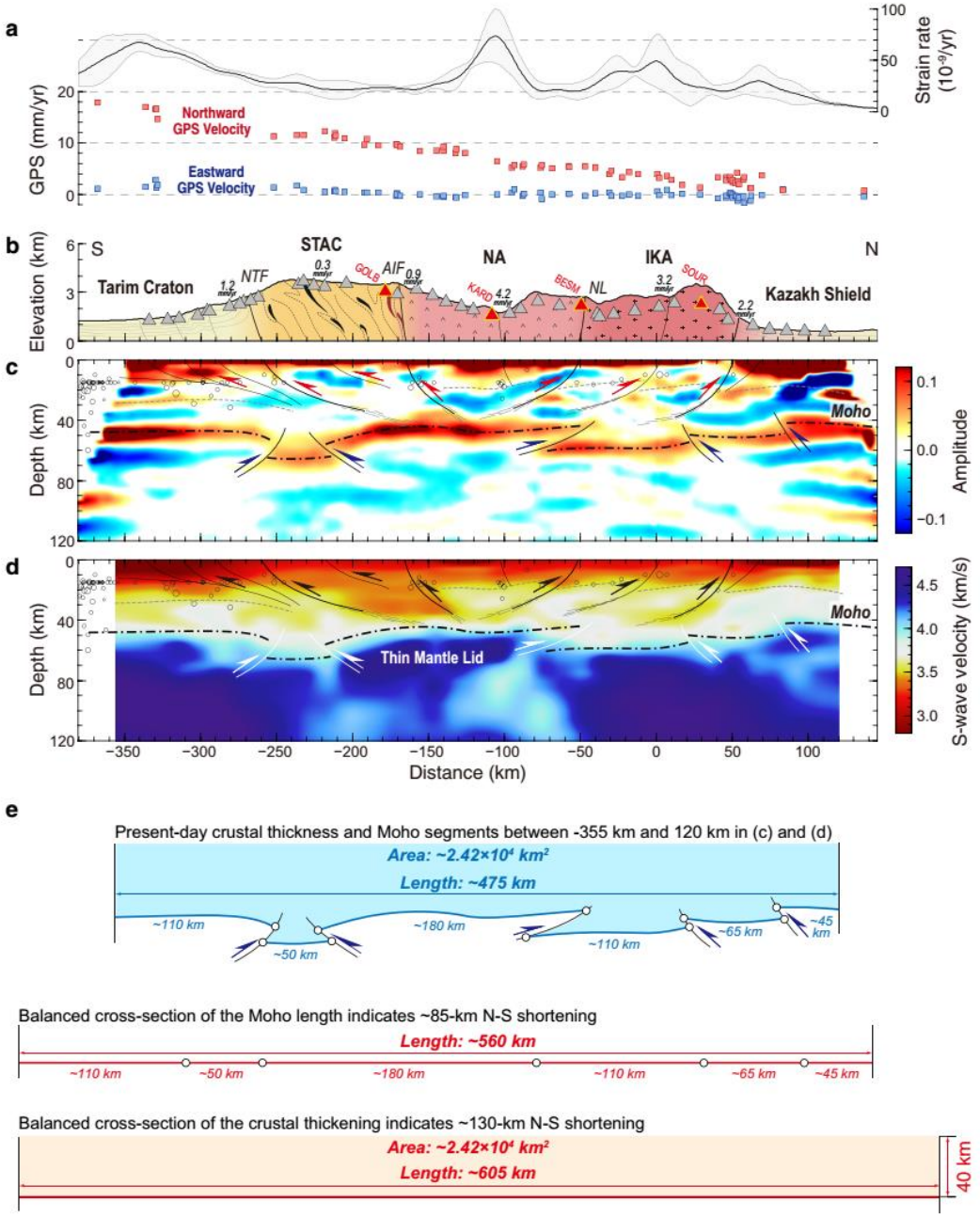

Figure 2. Interpreted seismic images and balanced cross-sections across the central Tianshan. a Strain rates37 and GPS velocities70 along the cross-section. The bold black line and gray-filled area indicate the averaged strain rates and corresponding standard deviations within a 1.0-degree width corridor centered by the cross-section. The individual GPS observations within the corridor are projected onto the cross-section as blue squares for eastward components and red squares for northward components. b Schematic geological cross-section across the Tianshan showing major tectonic units (modified after Xiao et al.4) and the slip rates of main faults28,69. Triangles represent stations used in this study, and red ones with marks indicate four stations chosen as examples showing the joint inversion in Supplementary Figs. 4 and 5. AIF Atbashy-Inylchek Fault, IKA Issyk Kul Arc, NA Naryn Arc, NL Nikolaev Line, NTF North Tarim Fault, STAC South Tianshan Accretionary Complex. c, d The CCP stacking image with a Gaussian coefficient of 2.0 and the VS model were obtained from joint inversion in this study. These are plotted with interpreted faults (solid lines), Conrad (dashed thin lines) and Moho (dashed thick lines) discontinuities. Gray circles denote earthquakes located within a 50-km width corridor centered by the cross-section65. e Estimates of N–S shortening in the Tianshan based on the balanced cross-sections of the Moho length and crustal thickening.

3. 人工沉积物中通过纤铁矿的固态转化形成胶黄铁矿

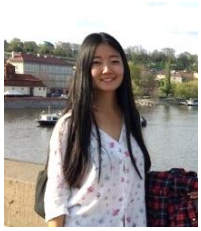

翻译人：张琪 zhangq7@sustech.edu.cn

Roud S C, Gilder A A, Park S. ***Greigite (Fe_3S_4) formation in artificial sediments via solid-state transformation of lepidocrocite*** *[J] Geochemistry, Geophysics, Geosystems, 2022, e2022GC010376.*

https://doi.org/10.1029/2022GC010376

摘要：胶黄铁矿(Fe_3S_4)是一种具有亚铁磁性的硫化铁矿物，在沉积物的成岩作用下形成。胶黄铁矿出现在年续堆积的地层剖面中，使环境记录和古地磁记录变得复杂。古地磁和岩石磁学研究的一个重要目标是确定胶黄铁矿的存在及其形成条件。然而，由于样品粒度的准确稳定性与质地纯度等的缺乏，胶黄铁矿的检测依然存在挑战性，其岩石磁学性质也十分模糊。为了克服这些限制，本文报告了一种新的方法，选择性的以四方硫铁矿（FeS）为中间物质将鳞屑石转化为胶黄铁矿。在不同底质的离散样品上进行原位磁性特征测量。结果显示磁化率和化学剩磁随时间成比例增加，定义了两种不同的胶黄铁矿生长模式。初始生长速率随温度的变化而变化，表示为固态的 FeS 向胶黄铁矿的转化，其活化能为 78-90 kJ/mol。超顺磁(SP)和单畴(SD)颗粒胶黄铁矿的低温以及室温剩磁和矫顽力与计算得到的曲线相吻合，在 300 K 和 100 K 时，SD 的剩磁和矫顽力的比例分别为 25%和 50%。这一趋势与此前关于天然胶黄铁矿沉积物的经验数据相一致，表明端元尺寸为 5-10 nm 的 SP 可能来自于四方硫铁矿结晶。x 射线粉末衍射和电子显微镜测得的平均粒径为 20 ~ 50 nm，与理论预测的胶黄铁矿 SP/SD 阈值尺寸一致。该方法为合成胶黄铁矿和研究其在沉积物中的形成提供了一种新的方法。

ABSTRACT: Greigite (Fe_3S_4) is a ferrimagnetic iron-sulfide mineral that forms in sediments during diagenesis. Greigite growth can occur diachronously within a stratigraphic profile, complicating or overprinting environmental and paleomagnetic records. An important objective for paleo- and rock-magnetic studies is to identify the presence of greigite and to discern its formation conditions. Greigite detection remains, however, challenging and its magnetic properties obscure due to the lack of pure, stable material of well-defined grain size. To overcome these limitations,

we report a new method to selectively transform lepidocrocite to greigite via the intermediate phase mackinawite (FeS). In-situ magnetic characterization was performed on discrete samples with different sediment substrates. Susceptibility and chemical remanent magnetization increased proportionally over time, defining two distinct greigite growth regimes. Temperature dependent and constant initial growth rates indicate a solid-state FeS to greigite transformation with an activation energy of 78-90 kJ/mol. Low and room temperature magnetic remanence and coercivity ratios match with calculated mixing curves for superparamagnetic (SP) and single domain (SD) greigite and suggest ~25% and ~50% SD proportions at 300 K and 100 K, respectively. The trend coincides with empirical data reported for natural greigite-bearing sediments, suggesting a common SP endmember size of 5-10 nm that is likely inherited from mackinawite crystallites. The average particle size of 20-50 nm determined by X-ray powder diffraction and electron microscopy accords with theoretical predictions of the SP/SD threshold size in greigite. The method constitutes a novel approach to synthesize greigite and to investigate its formation in sediments.

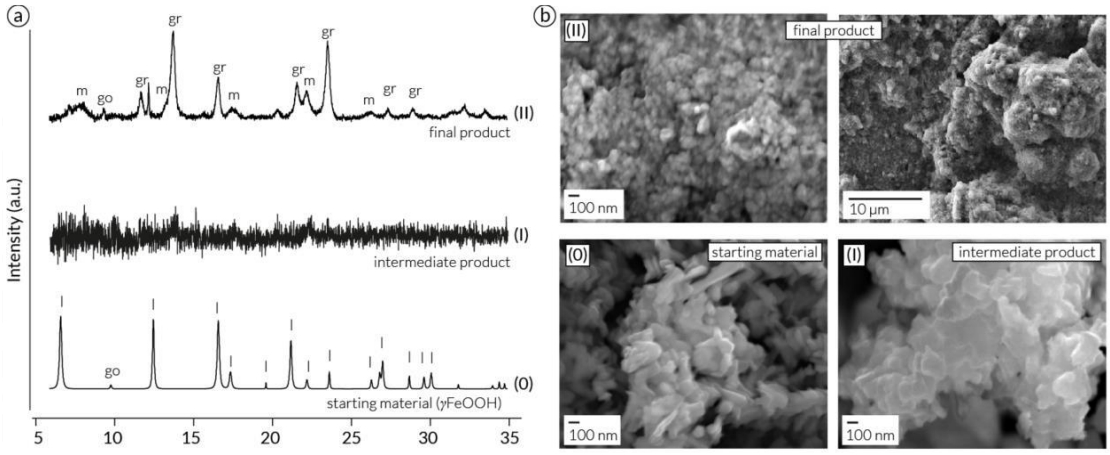

Figure 1. Starting material and transformation products. (a) XRD data and (b) SEM images of the starting material γ– FeOOH (0), the intermediate product (Step I) and the final product (Step II). The XRD pattern of the starting material indicates that lepidocrocite (l) is the main phase along with trace amounts of goethite (go). The XRD pattern for the sample from Step II has reflections indicative of greigite (gr) and mackinawite (m) as the main phases.

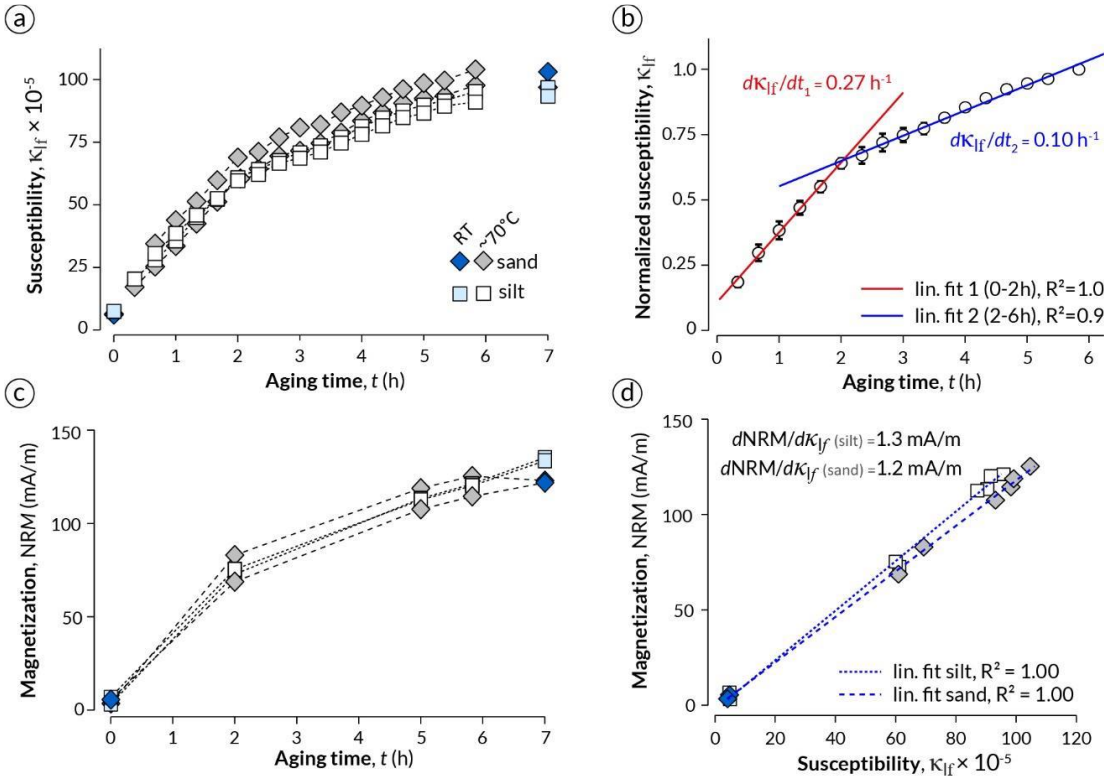

Figure 2. Greigite growth and grain size characterization. (a) Low-frequency magnetic susceptibility κ_{lf} against aging time (t, in hours). Measurements during the experiment (gray and open symbols) were performed on samples close to 70 ℃; the initial and final data points (blue) were measured at room temperature. (b) Mean and standard deviation (n = 4) of normalized κ_{lf} curves with average susceptibility growth rates $d\kappa_{lf}/dt$. (c) Natural remanent magnetization, NRM against aging time (t, in hours). (d) NRM against κ_{lf} demonstrating a linear correlation (R^2 = 1.00) among sand and silt samples. A magnetic field of 100 μT was applied in all cases. Diamonds and squares represent sand (#100-03 and -04) and silt samples (#100-10 and -11), respectively.

4. 中国近海盆地新生代构造演化及其对东亚大陆边缘地球动力学过程的响应

翻译人：刘伟 inewway@163.com

Cheng Y, Wu Z, Zhang J, et al. ***Cenozoic tectonic evolution of offshore Chinese Basins and its response to geodynamic processes of the East Asian Continental Margin*** *[J] Earth-Science Reviews, 2022.*

https://doi.org/10.1016/j.earscirev.2022.104140

摘要：中国近海盆地位于东亚板块向西太平洋板块的过渡地带。这些盆地新生代的演化反映了东亚地区的地球动力学过程。然而，对中国近海盆地的演化与东亚大陆边缘发生的地球动力学过程的耦合仍知之甚少。本文利用地震数据、断层活动、同沉积断裂图和等厚图分析了中国近海盆地的裂陷作用过程以及盆地演化与东亚板块地球动力学过程之间的关系。渤海湾盆地在近海同时发生了区域伸展和局部剪切作用。因此，区域 NNW-SSE 向伸展和局部 NNE 向走滑作用导致了辽东湾地区 NNE 向地堑-地垒构造，而 NW 向伸展断裂和 NNE 向扭张断裂共同控制了渤中地区的构造。此外，郯庐断裂带 NNE 向分支在渤南地区形成拉分构造，NW 向正断层控制了渤西地区的半地堑构造。东海盆地裂陷中心向东迁移的两个阶段分别是由太平洋板块俯冲方向在~43 Ma 发生变化和菲律宾海板块在~20 Ma 俯冲导致的。在南海，古新世至早始新世的初始伸展发生在目前的南海北部和南部边缘盆地中。随后，哀牢山红河剪切带穿过中印地块的东缘，并导致沿该断层附近的盆地以拉分裂陷作用为主。古南海板片的南移和哀牢山红河剪切带的走滑运动，南海海底发生扩张，南部边缘盆地从 33-16 Ma 远离华南地块向南漂移。

ABSTRACT: The offshore Chinese basins are located in the transition zone from the East Asia to the Western Pacific plate. The Cenozoic evolution of these basins reflects the geodynamic processes in East Asia. However, the coupling of the evolution of the offshore Chinese basins to the geodynamic processes occurring in the East Asian continental margin is still poorly understood. Here, the rifting processes of the offshore Chinese basins and the relationship between the basin evolution and the geodynamic processes of the East Asia Plate were analyzed using seismic data,

fault activity, syn-sedimentary fault maps, and isopach maps. In the Offshore Bohai Bay Basin, the regional extension and local shearing occurred simultaneously. Accordingly, the regional NNW-SSE extension and local NNE-strike-slip shearing resulted in the NNE-striking graben-horst structure in the Liaodong Bay area while the NW-striking extensional faults and NNE-striking transtensional faults jointly control the structure of the Bozhong area. In addition, the NNE-striking branches of the Tan-lu Fault Zone led to the pull-apart structure in the Bonan area, and the NW-striking normal faults governed the half-graben structure in the Boxi area. Two stages of eastward movement of the rifting center in the East China Sea Basin were triggered by a change in the direction of subduction of the Pacific plate at ~43 Ma, and subduction of the Philippine Sea plate at ~20 Ma, respectively. In the South China Sea (SCS), Paleocene to E. Eocene initial extension occurred in the present northern and southern marginal basins of the SCS. Subsequently, the Ailao Shan Red River shear zone (ASRRSZ) traversed the eastern margin of the Indochina block, and pull-apart rifting dominated in the basins along this fault. Combined with the southward slab pull of proto-SCS and the strike-slip movement of ASRRSZ, sea floor spreading occurred, and the southern marginal basins drifted southerly and apart from the South China from 33 to 16 Ma.

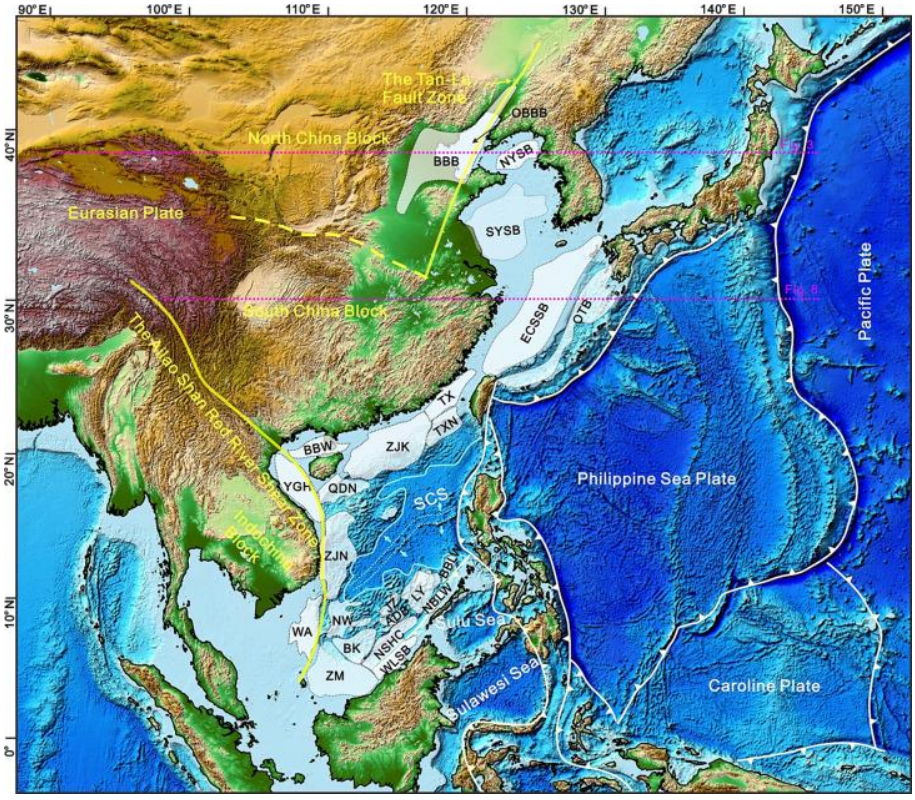

Figure 1. Map showing the regional tectonic framework of East and Southeast Asia, and locations of the Offshore Chinese basins.

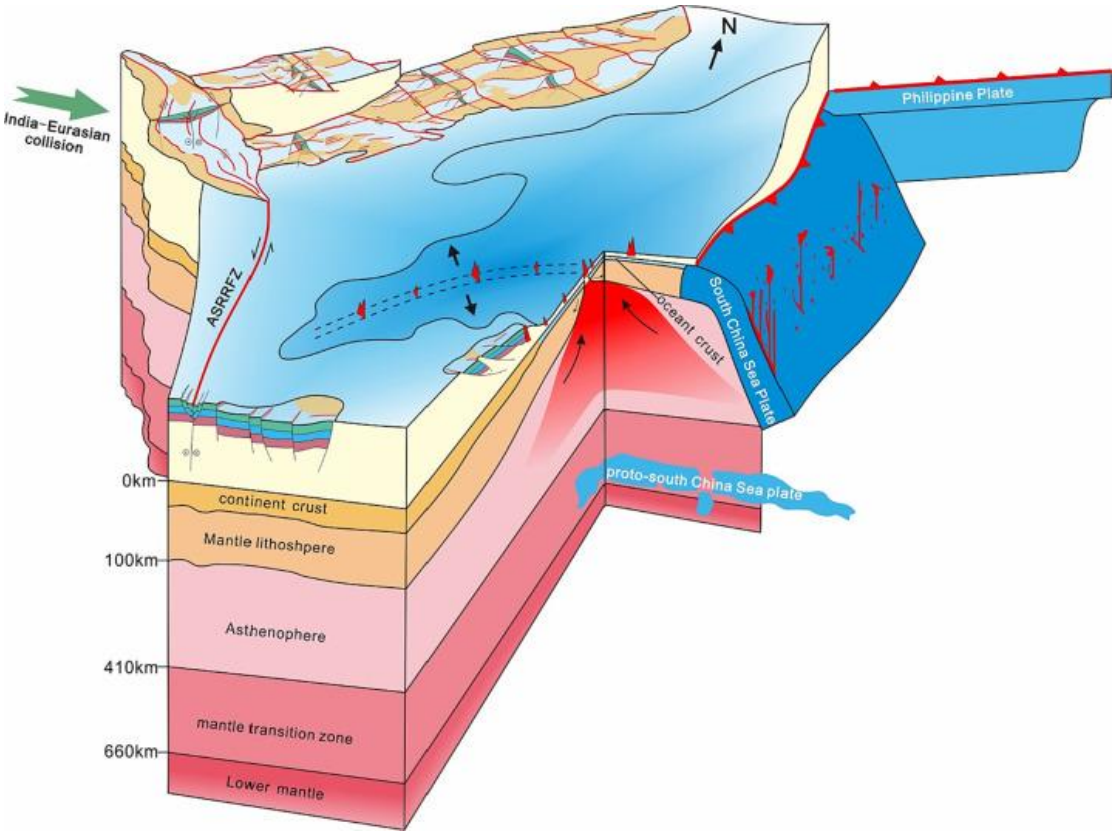

Figure 2. Structural model in the South China Sea showing the relationship between the structure of South China Sea Shelf basins and the deep structure of related plates.

5. 对流层中高层季节内气候振荡及其对东亚西风急流和中国东部雨带北移的影响

翻译人：杨会会 11849590@mail.sustech.edu.cn

Li J Y, Liu B Q, Mao J Y, X X. ***Climatological intraseasonal oscillation in the middle–upper troposphere and its effect on the northward migration of the East Asian westerly jet and rain belt over eastern China*** *[J] International Journal of Climatology, 2021, 41, 5084–5099. https://doi.org/10.1002/joc.7118*

摘要：利用1981-2010年逐日大气环流资料，确定了对流层中高层的季节内气候振荡(CISO)，揭示了CISO对梅雨季出现在6月中旬至7月中旬的时期以及东北地区7月下旬开始的降雨期的关键作用。小波分析表明，北半球夏季200-和500-hPa的气候纬向风存在显著的20-90天的周期，表明对流层中高层存在纬向风的CISO。纬向风CISO的主导模态在东亚沿海呈偶极子型，表明其受中国东南部和西北太平洋(SC-WNP)对流控制。6月中旬，SC-WNP上空受抑制对流作用，形成向极倾斜的强反气旋，主导WNP上空。因此，更多的水汽输送到长江流域中下游；同时，也导致了对流层中层(上层)东亚西风急流(EAWJ)向32°N(36°N)以北移动，这增强了暖平流层和对流层上层的辐散，进一步增加了长江流域降水，从而促进了梅雨季的启动。7月中旬，活跃对流取代了SC-WNP上空的抑制对流，环流格局逆转从而结束了梅雨季节。7月下旬，活跃对流由赤道向热带西太平洋转移，导致纬向风CISO的第二模态出现，其特征是对流层中高层出现准正压蒙古反气旋。对流层上层的EAWJ进一步移动到45°N，诱导对流层上层辐散向北移，从而启动了东北地区的降雨期。

ABSTRACT: Using daily atmospheric circulation data for 1981–2010, we identify the climatological intraseasonal oscillation (CISO) in the mid-upper troposphere and reveal its critical role in anchoring the Meiyu season to the period from mid-June to mid-July and the rainfall episode of northeastern China to begin in late July. Wavelet analysis shows a significant 20-90-day period in the climatological 200- and 500-hPa zonal winds during boreal summer, indicating the existence of the zonal wind CISO in the mid–upper troposphere. The leading mode of zonal wind CISO features a dipole pattern along the coast of East Asia controlled by convection over the southeastern

China-western North Pacific (SC-WNP). In mid-June, suppressed convection over the SC-WNP induces the negative phase of intraseasonal Pacific–Japan pattern, leading to the strong anticyclone with a poleward tilt with height to dominate over the WNP. Consequently, more moisture are transported to the middle and lower reaches of the Yangtze River Valley (YRV), and the mid-tropospheric (upper-tropospheric) East Asian westerly jet (EAWJ) is shifted north of 32°N (36°N), which further increases the YRV rainfall through enhancing warm advection and upper-tropospheric divergence, thus facilitating the initiation of Meiyu season. In mid-July, active convection occupies the SC-WNP instead, with the reversed circulation pattern terminating the Meiyu season. In late July, active convection shifts from the equator to the tropical western Pacific, leading to the second mode of zonal wind CISO, which is characterized by a quasi-barotropic Mongolian anticyclone in the mid-upper troposphere. The upper-tropospheric EAWJ is further shifted to 45°N, displacing the induced upper-tropospheric divergence northward, thus initiating the rainfall episode of northeastern China.

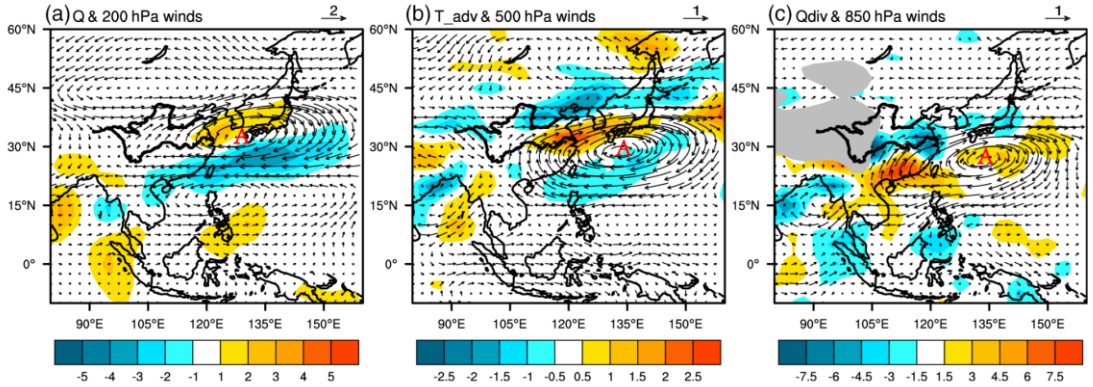

Figure 1. (a) Climatological intraseasonal components of (a) the vertically integrated (100^{-1},000 hPa) diabatic heating (color scale, 10^3 W m^{-2}) and 200-hPa winds (m s^{-1}), (b) 500-hPa horizontal temperature advection (color scale, 10^{-1} K d^{-1}) and winds (m s^{-1}), (c) 850-hPa specific humidity convergence (color scale, 10^{-9} s^{-1}) and winds (m s^{-1}) regressed against the CISO1 index during the boreal summer (May 1 to August 31) of 1981-2010. The magnitude of the reference vector is provided at the bottom right. The thickened curves show the locations of the Yangtze and Yellow Rivers, with the southern curve indicating the Yangtze River and the northern one denoting the Yellow River. The grey shading refers to the Tibetan Plateau with terrain altitude above 1,500 m [Color figure can be viewed at wileyonlinelibrary.com]

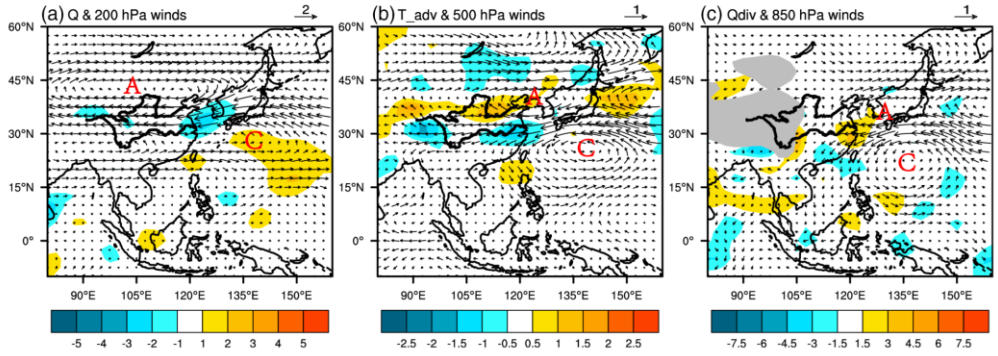

Figure 2. (a) As in Figure 1, but for the results regressed against the CISO2 index [Color figure can be viewed at wileyonlinelibrary.com]

6. 多硫同位素约束谢尔普霍夫阶大灭绝期间的环境变化

翻译人：张靖宇 zhangjy6@sustech.edu.cn

Hu D, Li M, Zhang X, et al. ***Multiple S-isotope constraints on environmental changes during the Serpukhovian mass extinction*** *[J] Earth and Planetary Science Letters, 2022, 594, 117719. https://doi.org/10.1016/j.epsl.2022.117719*

摘要：根据其生态影响，谢尔普霍夫阶（石炭纪中期）大灭绝在主要的显生宙生物多样性危机中排名第五。晚古生代冰期（LPIA）驱动的全球变冷和环境恶化被认为是谢尔普霍夫阶大灭绝的潜在驱动因素；然而，潜在的灭绝机制仍然不为人所知。在此，我们展示了华南地区纳庆剖面的黄铁矿多 S 同位素记录（$\delta^{34}S$ 和 $\Delta^{33}S$），纳庆剖面是谢尔普霍夫阶底部的潜在全球层型剖面（GSSP）。我们的研究结果揭示了负 $\Delta^{33}S$ 和 $\delta^{34}S$ 值的独特 S-同位素特征，揭示了石炭纪中期海洋的氧化还原变化。S-同位素组成的混合信号表明深层缺氧水对浅水陆架的入侵。在谢尔普霍夫阶灭绝期间，S-同位素混合信号的重现，表明海洋氧化还原条件的不稳定性，有毒缺氧水的偶发入侵可能是谢尔普霍夫阶灭绝的原因。

ABSTRACT: The Serpukhovian (mid-Carboniferous) mass extinction has been ranked fifth among the major Phanerozoic biodiversity crises, based on its ecological impact. Global cooling and environmental deterioration driven by the late Paleozoic ice age (LPIA) have been invoked as potential drivers of the Serpukhovian extinction; however, the underlying killing mechanisms remain poorly understood. Here we present multiple S-isotopic records ($\delta^{34}S$ and $\Delta^{33}S$) of pyrites from the Naqing section in South China, a potential Global Stratotype Section and Point (GSSP) for the base of the Serpukhovian Stage. Our results reveal the distinctive S-isotopic characteristics of negative $\Delta^{33}S$ and $\delta^{34}S$ values, implying changes in redox conditions in the mid-Carboniferous oceans. The mixing signal of S-isotopic compositions suggests the encroachment of deep anoxic water onto the shallow shelves. The recurrence of the S-isotope mixing signal during the Serpukhovian extinction suggests the instability of oceanic redox conditions and that the episodic incursion of toxic anoxic water may have contributed to the Serpukhovian extinction.

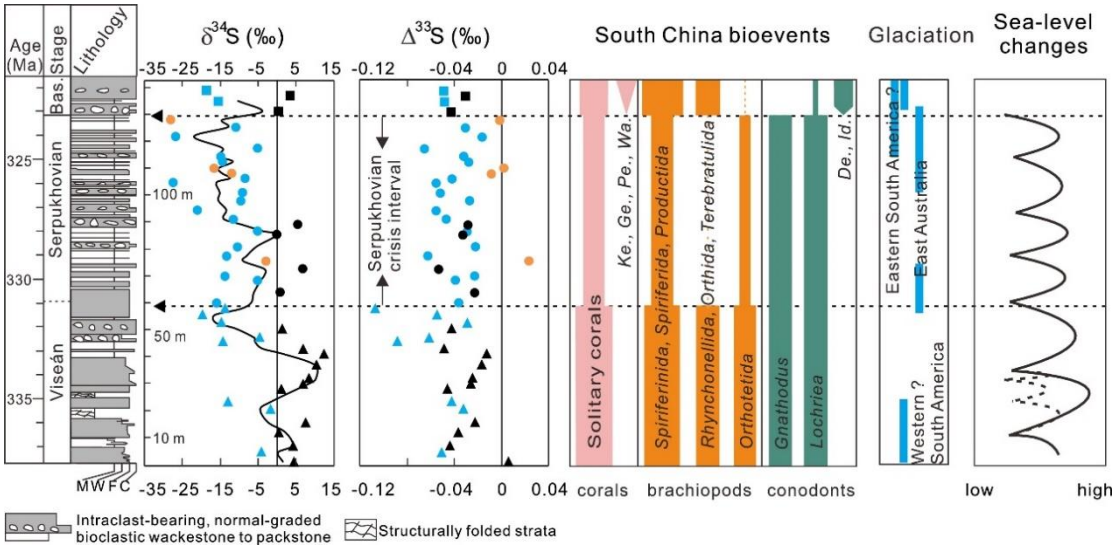

Figure 1. Compilation of chronostratigraphy, multiple S-isotopic data, bio-events, and sea-level changes in South China across the Viseán – Serpukhovian boundary. The stratigraphy of the Naqing section and inferred sea-level changes are modified from Chen et al. (2019), the bio-events in South China are based on Wang et al. (2006, 2013) and Shen et al. (2006), and the temporal distribution of glaciation is based on Chen et al. (2018) and references therein. Triangles, circles, and rectangles represent data for the intervals before, during, and after the Serpukhovian extinction, respectively. The orange, blue, and black colors of the data symbols respectively indicate S-isotopic compositions located in quadrants II, III, and IV in Fig. 3. The black solid curve shows moving averages over three consecutive $\delta^{34}S$ values. Bas.-Bashkirian; M-lime mudstone; W-wackestone; F-fine packstone; C-coarse packstone. Ke.-Kepingophyllidae; Ge-Geyerophyllidae; Pe.-Petalaxidae; Wa.-Waagenophyllidae; De.-Declinognathodus; Id.-Idiognathoides.

7. 太阳活动引发的亚洲夏季风全新世百年变化

翻译人：王浩森 11930841@mail.sustech.edu.cn

Sun W, Liu J, Wang B, et al. ***Holocene multi-centennial variations of the Asian summer monsoon triggered by solar activity*** *[J] Geophysical Research Letters, 2022, e2022GL098625. https://doi.org/10.1029/2022GL098625*

摘要：太阳活动在不同时间尺度上影响亚洲夏季风 (ASM)。然而，在百年时间尺度上，太阳活动是否以及如何影响 ASM 仍不得而知。利用地球系统模型，我们进行了加速因子为 10 的太阳活动驱动全新世的瞬态模拟，结果表明，在中-晚全新世期间，在太阳驱动下，ASM 降水表现出显著的 300-600 年周期性。各参数数据也提出了这种产生百年变化的模型。多个百年 ASM 变化的主导模式显示出“湿热带-干亚热带”模式，其将相应的太阳活动滞后约四分之一个周期。西北太平洋环流系统通过加强南亚-西北太平洋季风槽的气候作用，导致了长达数百年的 ASM 变化。我们认为，太阳活动调节了热带太平洋的纬向 SST 梯度，诱发了异常西太平洋气旋，并以延迟模式增强了 ASM 降水。

ABSTRACT: Solar activity affects Asian summer monsoon (ASM) at various time scales. However, it remains unknown if and how solar activity can influence ASM on the centennial time scale. Using the Community Earth System Model, we conduct a solar activity forced Holocene transient simulation with an acceleration factor of 10 and show that during the middle–late Holocene ASM precipitation exhibits a significant 300–600-year periodicity under solar forcing. This model-produced multi-centennial variation is also suggested by proxy data. The leading mode of the multi-centennial ASM variation shows a “wet tropics–dry subtropics” pattern, which lags the corresponding solar activity by about a quarter cycle. The western North Pacific (WNP) circulation system is responsible for the multi-centennial ASM variation, through enhancing the climatological south Asia–WNP monsoon trough. We suggest that solar activity modulates the zonal SST gradients of the tropical Pacific, inducing the anomalous WNP cyclone and enhancing ASM precipitation in a delayed mode.

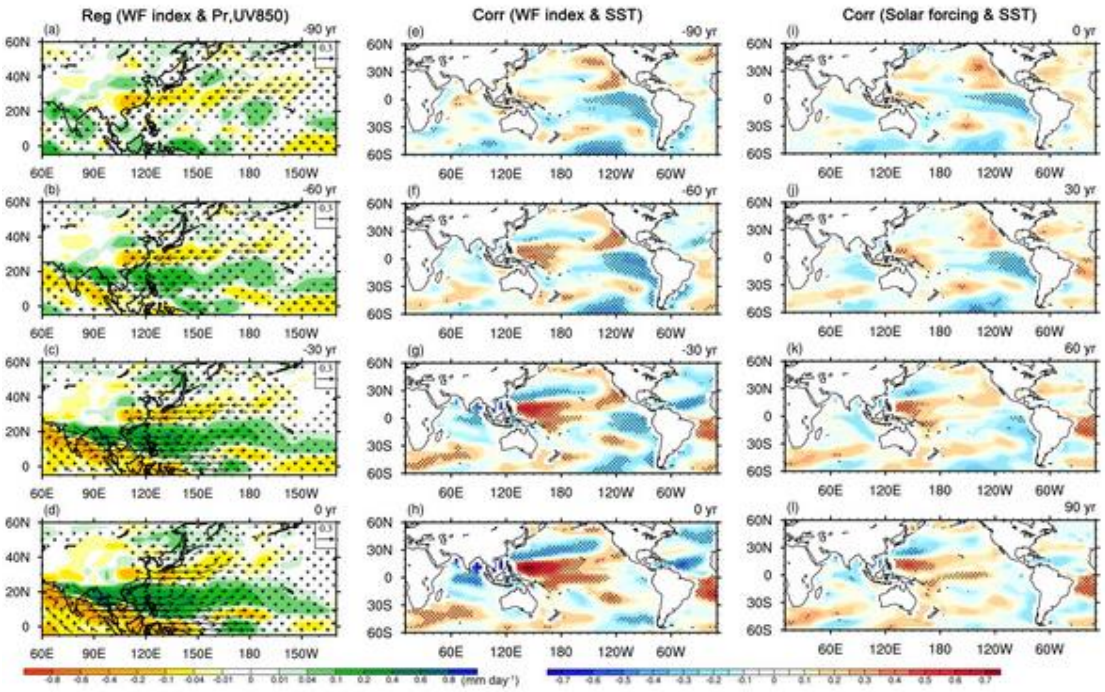

Figure 1. The spatial evolution of Asian summer monsoon (ASM) and the associated sea surface temperature (SST) pattern. (a–d) Regressed June–July–August (JJA) mean precipitation (mm day^{-1}, shading) and 850 hPa winds (m s^{-1}, vectors) on the normalized WF index. The labels "−30 years," "−60 years," and "−90 years" denote that the WF index lags precipitation and winds by 30, 60, and 90 years, respectively. Only the significant results with confidence levels exceeding 90% (two-tailed Student's *t*-test) are displayed. (e–h) Correlation maps of JJA mean SST (°C, shading) with the WF index. The dots denote results that are significant at the 90% confidence level (*r* test). (i–l) Correlation maps of JJA mean SST (°C, shading) with the solar forcing. The labels "30 years," "60 years," and "90 years" denote that the solar forcing leads SST by 30, 60, and 90 years, respectively.

8. 内蒙古渐新世湿度变化的风尘序列证据

翻译人：王敦繁 Dunfan-w@foxmail.com

Wasiljeff J, Salminen J M, Stenman J, et al. ***Oligocene moisture variations as evidenced by an aeolian dust sequence in Inner Mongolia, China*** *[J] Scientific reports, 2022, 12, 5597. https://doi.org/10.1038/s41598-022-09362-y*

摘要：始新世以来中亚地区的干旱化已经有了广泛的证据，但渐新世时期气候控制的环境重仍不明确。本研究利用环境磁学、矿物学和地球化学方法对内蒙古始新世至晚渐新世陆相层序进行了研究，探讨了全球气候变化趋势和区域因子对内蒙古地区水汽和风化的影响。我们的风化和降雨代理数据突出了气候的影响，记录了早渐新世半干旱阶段大气 CO_2 的下降和全球变冷，并在 31 Ma 的早渐新世干旱化事件中达到顶峰。此外，首次在陆相中亚东部背景下，提供了与中渐新世最大冰期(约 28 Ma)几乎同步的第二次渐新世干旱化事件的地球化学和地球物理证据。这些被增强的降雨和风化事件打断的干旱化记录，可以在海洋氧同位素记录中看到冰川事件的终止。

ABSTRACT: The aridification of Central Asia since the Eocene has widespread evidence, but climate-controlled environmental reorganizations during the Oligocene remain ambiguous. We employed environmental magnetic, mineralogical and geochemical methods on a latest Eocene to late Oligocene terrestrial sequence in Inner Mongolia, China, to examine how global climatic trends and regional factors influenced the evolution of moisture and weathering in the region. Highlighting the climatic influence, our weathering and rainfall proxy data document the drawdown of atmospheric CO_2 and global cooling during the early Oligocene semi-arid phase, which culminated in the Early Oligocene Aridification Event at 31 Ma. Moreover, for the first time in the terrestrial eastern Central Asian setting, we provide geochemical and geophysical evidence for a second major Oligocene aridification event nearly synchronous to the mid-Oligocene Glacial Maximum at around 28 Ma. These aridification events were interrupted by periods of increased rainfall and weathering and can be associated with the terminations of glacial events seen in marine oxygen isotope records.

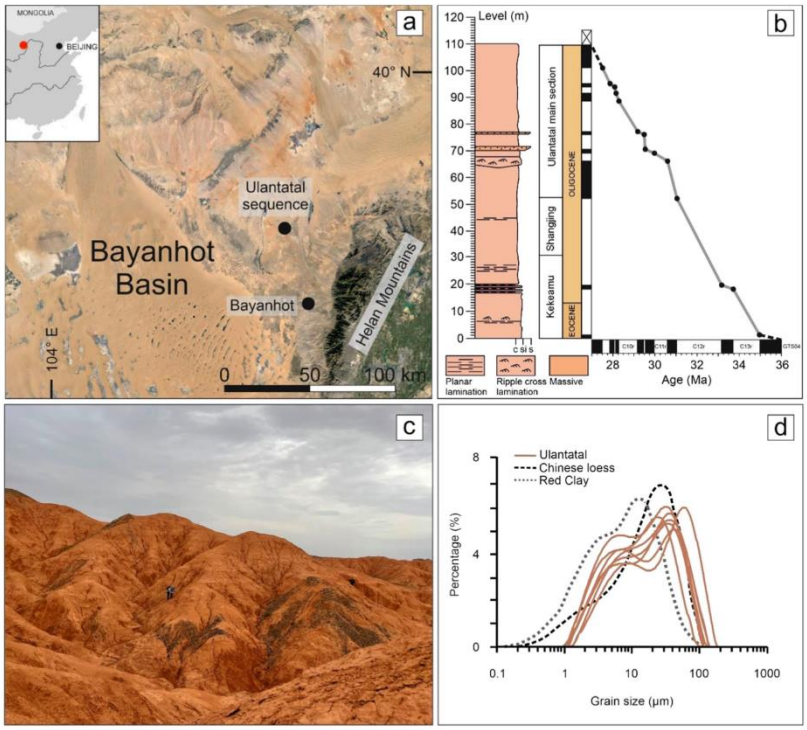

Figure 1. (a) A regional Google Earth Pro map (www.google.com/intl/en/earth) of the Bayanhot Basin, also showing the location of the studied Ulantatal sequence. The satellite image was modified with CorelDRAW 2020 (www.coreldraw.com) (b) A simplified lithological column of the Ulantatal sequence with subsections, sediment thickness, epochs and age-depth model. c Field view from the Kekeamu section where alternating more yellowish versus more reddish beds are visible. (d) Grain size distributions of selected samples from Ulantatal in comparison to Chinese loess and Red Clay.

9. 低 Ti 与高 Ti 岩浆氧化状态差异控制了峨眉山大火成岩省 Ni-Cu 硫化物与 Fe-Ti 氧化物的矿化

翻译人：张伟杰 12031188@mail.sustech.edu.cn

Cao Y, Wang C Y. ***Contrasting oxidation states of low-Ti and high-Ti magmas control Ni-Cu sulfide and Fe-Ti oxide mineralization in Emeishan Large Igneous Province*** *[J] Geoscience Frontiers, 2022, 101434.*

https://doi.org/10.1016/j.gsf.2022.101434

摘要：地幔柱相关的大火成岩省岩浆 Ni-Cu-(PGE)硫化物和 Fe-Ti 氧化物矿床通常分别与低钛和高钛系列岩浆有关，但控制成矿类型和岩浆成分关系的主要因素尚不清楚。岩浆 *f*O2 控制着镁铁质岩浆中硫的状态和铁钛氧化物饱和的相对时间，可能有助于上述问题的解决。以峨眉山 LIP 为例，利用橄榄石-尖晶石氧压力计，计算了高钛和低钛苦橄岩岩浆的 *f*O2，以及橄榄石中 V 的配分。高 Ti 系列岩浆（FMQ+1.1～FMQ+2.6）获得的 *f*O2 高于低 Ti 系列岩浆（FMQ-0.5～FMQ+0.5）。含 Fo＞90 橄榄石的高 Ti 和低 Ti 苦橄榄岩的岩浆 *f*O2 表明，高 Ti 系列的地幔源区可能比低 Ti 系列氧化程度更高。使用“lambda REE”方法的结果表明，高钛系列可能来自相对氧化的地幔，其中含有石榴石辉石成分。利用 alphaMelts 模型获得的液体成分计算了两个系列岩浆硫化物饱和度的 S 含量，结果表明，低 Ti 系列岩浆具有低 *f*O2，S 主要为 S^{2-}，容易达到硫化物饱和状态。相比之下，高 Ti 系列岩浆在 MgO 含量为~ 7.0 wt.%时，很难达到硫化物饱和，但可以结晶出 Fe-Ti 氧化物。因此，地幔柱相关的大火成岩省中低 Ti 和高 Ti 系列的岩浆 *f*O2 差异可能在形成两种不同类型的成矿过程中发挥重要作用。

ABSTRACT: Magmatic Ni-Cu-(PGE) sulfide and Fe-Ti oxide deposits in plume-related large igneous provinces (LIPs) are commonly related to low-Ti and high-Ti series magmas, respectively, but the major factors that control such a relationship of metallogenic types and magma compositions are unclear. Magma *f*O2 controls sulfur status and relative timing of Fe-Ti oxide saturation in mafic magmas, which may help clarify this issue. Taking the Emeishan LIP as a case, we calculated the magma *f*O2 of the high-Ti and low-Ti picrites based on the olivine-spinel oxygen barometer, and the partitioning of V in olivine. The obtained fO2 of the high-Ti series magma (FMQ + 1.1 to FMQ

+ 2.6) is higher than that of the low-Ti series magma (FMQ − 0.5 to FMQ + 0.5). The magma *f*O2 of the high-Ti and low-Ti picrites containing Fo > 90 olivine reveals that the mantle source of the high-Ti series is likely more oxidized than that of the low-Ti series. The results using the 'lambda REE' approach show that the high-Ti series may have been derived from relatively oxidized mantle with garnet pyroxenite component. The S contents at sulfide saturation (SCSS) of the two series magmas were calculated based on liquid compositions obtained from the alphaMelts modeling, and the results show that the low-Ti series magma could easily attain the sulfide saturation as it has low fO2 with S being dominantly as S^{2-}. In contrast, the oxidized high-Ti series magma is difficult to attain the sulfide saturation, but could crystallize Fe-Ti oxides at magma MgO content of ~7.0 wt.%. Thus, contrasting magma *f*O2 of low-Ti and high-Ti series in plume-related LIPs may play an important role in producing two different styles of metallogeny.

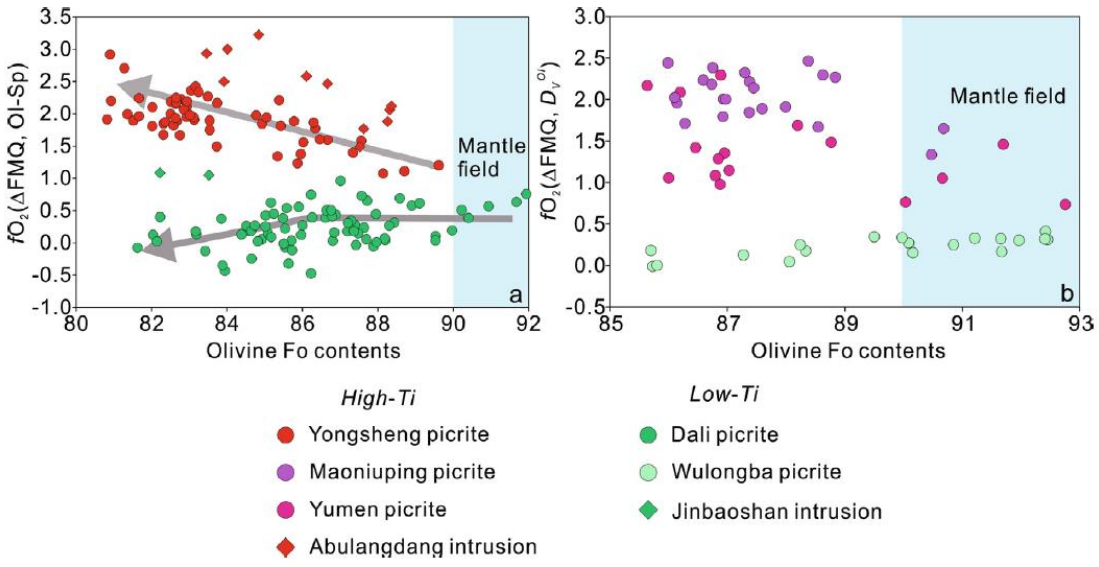

Figure 1. Plot of the Fo contents of olivine versus the magma *f*O2 calculated based on (a) the olivine-spinel oxygen barometer, and (b) the partitioning of V in olivine for the low-Ti and high-Ti series picrites and intrusions in the Emeishan LIP. The low-Ti and high-Ti series picrites and intrusions show opposite variation patterns in magma fO2 with the decreasing Fo contents of olivine. Data sources are the same as in Fig. 4.

10. 中上新世持续的温暖导致北太平洋深水的形成

翻译人：李海 12031330@mail.sustech.edu.cn

Ford H L, Burls N J, Jacobs P, et al. ***Sustained mid-Pliocene warmth led to deep water formation in the North Pacific*** *[J] Nature Geoscience, 2022.*

https://doi.org/10.1038/s41561-022-00978-3

摘要：持续温暖的地质时期，如中上新世暖期，可为我们了解未来的气候变化，包括海洋吸收人为碳的长期后果。在本研究中，作者构建碳同位素记录并结合现有记录来重建水团的位置，并确定太平洋深部的环流模式。研究结果表明，中上新世北太平洋中深部的碳同位素梯度与现今相比发生了逆转，指示洋流由北向南流动，深层水可能形成于亚北极北太平洋地区。同位素气候模型模拟重现了北太平洋深水区类似的碳同位素模式。模拟的北太平洋溶解无机碳含量水平略有下降，尽管由于表层海洋中溶解无机碳的增加，海洋中储存的碳量却比现代增加了 1.6%。尽管模拟的上新世海洋维持着于现代相似的碳收支，但深海环流结构的变化导致了下游生物地球化学的显著变化。

ABSTRACT: Geologic intervals of sustained warmth such as the mid-Pliocene Warm Period can inform our understanding of future climate change, including the long-term consequences of oceanic uptake of anthropogenic carbon. Here we generate carbon isotope records and synthesize existing records to reconstruct the position of water masses and determine circulation patterns in the deep Pacific Ocean. We show that the mid-depth carbon isotope gradient in the North Pacific was reversed during the mid-Pliocene compared with today, which implies water flowed from north to south and deep water probably formed in the subarctic North Pacific Deep Water. An isotopically enabled climate model that simulates this North Pacific Deep Water reproduces a similar carbon isotope pattern. Modelled levels of dissolved inorganic carbon content in the North Pacific decrease slightly, although the amount of carbon stored in the ocean actually increases by 1.6% relative to modern due to an increase in dissolved inorganic carbon in the surface ocean. Although the modelled Pliocene ocean maintains a carbon budget similar to the present, the change in deep ocean circulation configuration causes pronounced downstream changes in biogeochemistry.

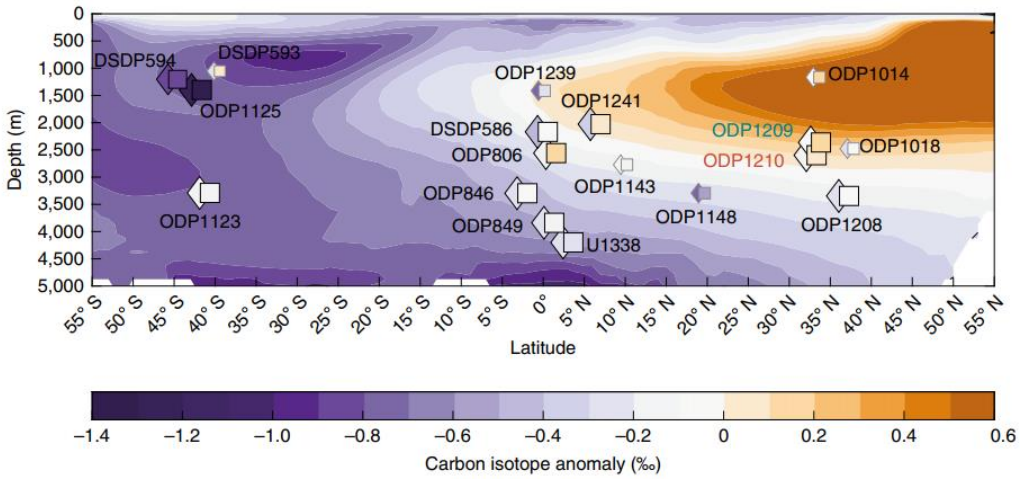

Figure 1. Observed benthic $\delta^{13}C$ and modelled zonal-mean anomalies for the mid-Pliocene Warm Period. The vertical cross section across the Pacific shows the core and spatial extent of the PMOC.

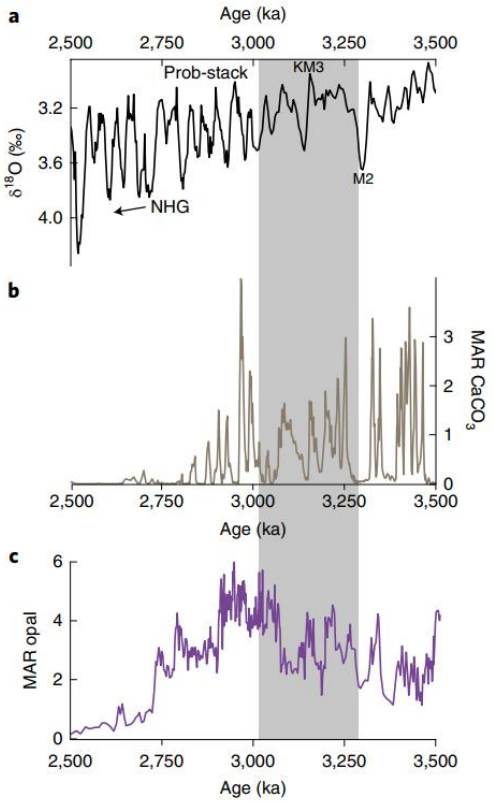

Figure 2. Benthic isotope records of Prob-stack and Site 882 sediment records $CaCO_3$ MAR and opal MAR. a, Benthic isotope records of a probabilistic Pliocene-Pleistocene stack (Prob-stack). b,c, Site 882 sediment records $CaCO_3$ mass accumulation rate (MAR) (b) and opal MAR (c).The grey shading indicates the mid-Pliocene Warm Period. Northern Hemisphere glaciation (NHG) and Marine Isotope Stages KM3 and M2 are labelled.

11. 东海内陆架泥质沉积物中沉积黄铁矿 C/S 比揭示了更新世-晚全新世的环境演变

翻译人：刘宇星 11811211@mail.sustech.edu.cn

Liu X, Zhang M, Li A, et al. ***Sedimentary pyrites and C/S ratios of mud sediments on the East China Sea inner shelf indicate late Pleistocene-Holocene environmental evolution*** *[J] Marine Geology, 2022, 106854.*

https://doi.org/10.1016/j.margeo.2022.106854

摘要：沉积黄铁矿和有机碳与黄铁矿硫的比值（C/S 比）已被广泛用作区分海洋和淡水环境的古盐度指标。然而，在具有反复强烈物理作用的不稳定海洋环境中，黄铁矿的形成是有限的，会导致较高的 C/S 比，就像在淡水环境中一样。因此，C/S 比值能否识别沉积地层中的不稳定海洋环境仍是一个有争议的话题。为了计算这些经典指标在不稳定环境中的可用性，我们分析了从东海内陆架获得的沉积物岩芯的多个指标。我们的研究结果表明，13.1 ka 之前在陆地条件下沉积的沉积物中没有黄铁矿聚集体。在此期间，C/S 比值高于 2.8，代表了沉积在淡水环境中的沉积物特征，这也得到了低 Sr/Ba 比的支持。当岩芯最初在约 13.1 ka 处受到海水入侵时，黄铁矿聚集体首次出现，并伴随着 C/S 比的快速下降，表明为半咸水滩涂环境。我们发现潮滩和内陆架环境之间的 C/S 比重叠，但内陆架沉积物中相对较高的黄铁矿聚集体和细粒沉积物含量可以有效地将这两种环境分开。我们的研究结果进一步表明，泥质沉积物的沉积中心最初在大约 7.5 ka 处形成，此时海平面达到高位。这些新发现表明，地球化学指标应始终与沉积和古生态证据结合使用，以防止得出有偏见的结论。

ABSTRACT: Sedimentary pyrite and the ratio between organic carbon and pyrite sulfur (C/S ratio) have been widely used as paleosalinity indicators to distinguish between marine and freshwater environments. However, in unsteady marine environments with strong physical reworking, the formation of pyrite is limited, leading to a high C/S ratio, as is the case in freshwater environments; thus, whether C/S ratios can identify unsteady marine environments in sedimentary strata is still a controversial topic. To calculate the availability of these classic indicators in unsteady environments, we analyzed multiple indicators of core sediments obtained from the inner shelf of the East China

Sea. Our results show that there are no pyrite aggregates in the sediments deposited under terrestrial conditions before 13.1 ka. During this period, the C/S ratios are higher than 2.8, representing the characteristics of sediment deposited in freshwater environments, which is also supported by low Sr/Ba ratios. When the core site was initially affected by seawater intrusion at approximately 13.1 ka, pyrite aggregates appeared for the first time, accompanied by a rapid decrease in C/S ratios, indicating a brackish tidal flat environment. We find that the C/S ratio overlaps between tidal flat and inner shelf environments, but the relatively high content of pyrite aggregates and fine-grained sediments in the shelf sediments can effectively separate these two environments. Our results further reveal that the mud depocentre initially developed at approximately 7.5 ka when the sea level reached its high stand. These new findings suggest that geochemical indicators should always be used in conjunction with sedimentary and paleoecological evidence to prevent biased conclusions.

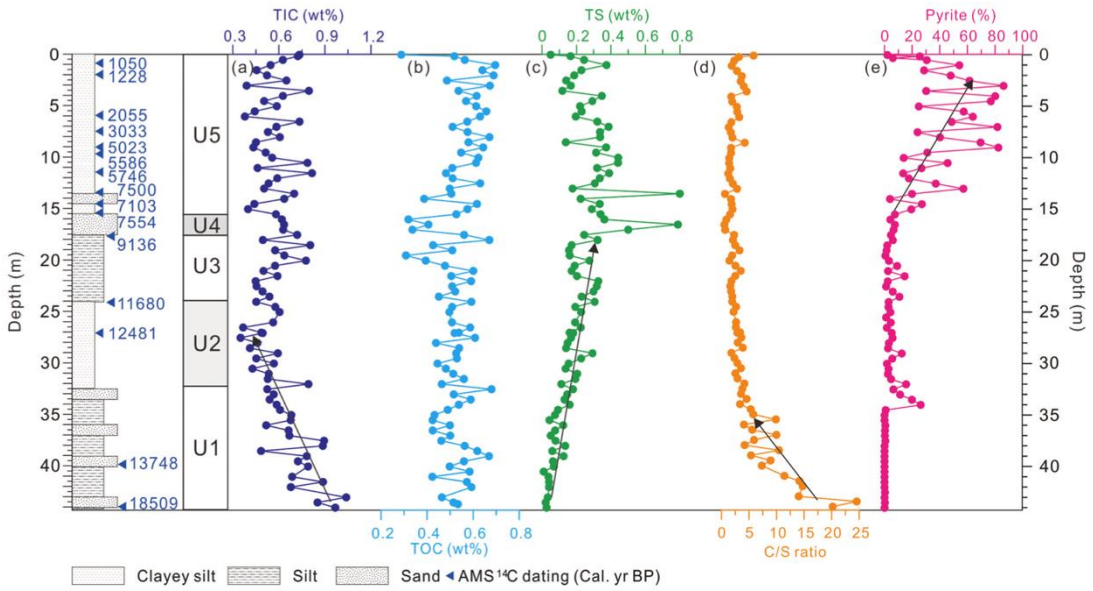

Figure 1. TIC, TOC and TS contents of core ECMZ. (a) TIC content; (b) TOC content; (c) TS content; (d) C/S ratio; (e) relative content of pyrite in hand-picked coarse-grained (coarser than 63 μm) heavy minerals.

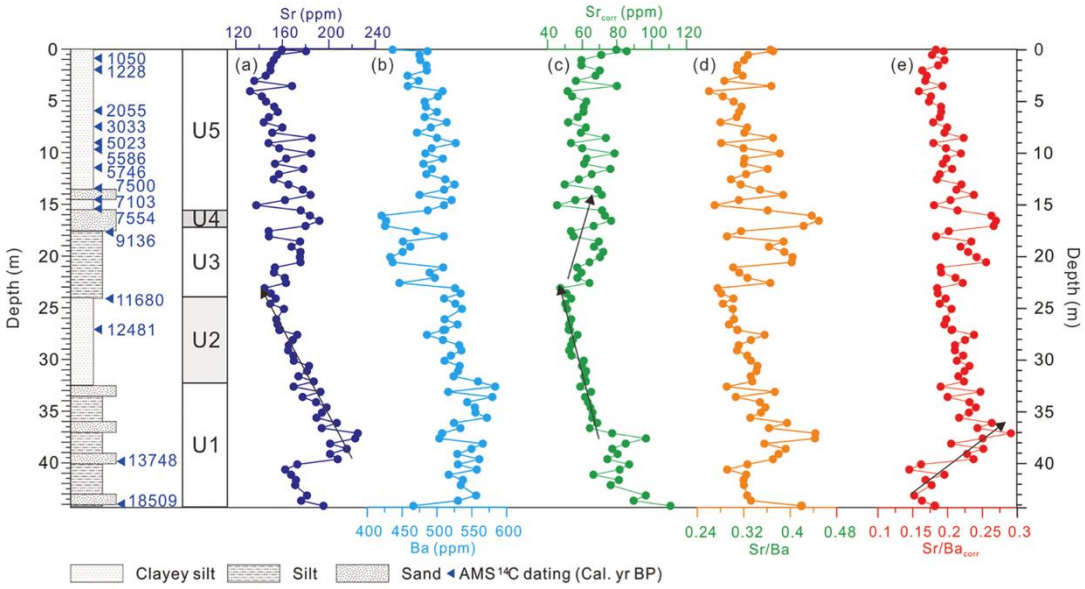

Figure 2. Sr and Ba contents and Sr/Ba ratios of core ECMZ. (a) Sr content; (b) Ba content; (c) corrected Sr content; (d) Sr/Ba ratio; (e) corrected Sr/Ba ratio.

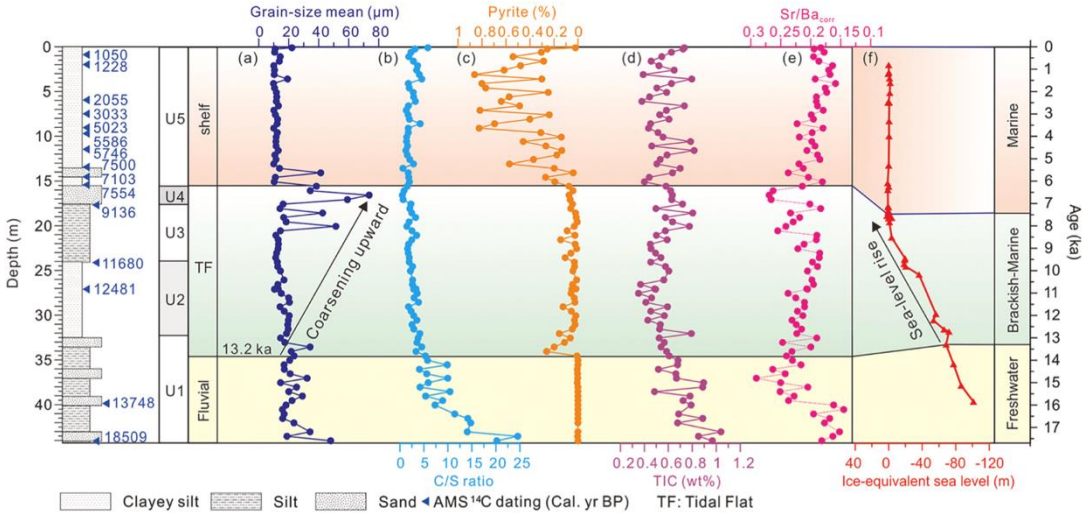

Figure 3. Sedimentary environmental evolution in response to deglacial sea-level rise. (a) Mean grain size; (b) C/S ratio; (c) hand-picked relative pyrite content in coarse (> 63 μm) heavy minerals; (d) TIC content, representing the carbonate components in the bulk sediments; (e) Sr/Ba_{corr}; (f) sea-level change since the last deglaciation (Lambeck et al., 2014).